

An informative path planning framework for UAV-based terrain monitoring

Marija Popović · Teresa Vidal-Calleja · Gregory Hitz · Jen Jen Chung · Inkyu Sa · Roland Siegwart · Juan Nieto

Received: date / Accepted: date

Abstract Unmanned aerial vehicles (UAVs) represent a new frontier in a wide range of monitoring and research applications. To fully leverage their potential, a key challenge is planning missions for efficient data acquisition in complex environments. To address this issue, this article introduces a general informative path planning (IPP) framework for monitoring scenarios using an aerial robot. The approach is capable of mapping either discrete or continuous target variables on a terrain using variable-resolution data received from probabilistic sensors. During a mission, the terrain maps built online are used to plan information-rich trajectories in continuous 3-D space by optimizing initial solutions obtained by a course grid search. Extensive simulations show that our approach is more efficient than existing methods. We also demonstrate its real-time application on a photorealistic mapping scenario using a publicly available dataset.

Marija Popović
E-mail: mpopovic@ethz.ch
Autonomous Systems Lab., ETH Zürich, Zürich, Switzerland

Teresa Vidal-Calleja
Centre for Autonomous Systems, University of Technology, Sydney, Australia
E-mail: teresa.vidalcallesja@uts.edu.au

Gregory Hitz
E-mail: hitzg@ethz.ch

Jen Jen Chung
E-mail: jenjen.chung@mavt.ethz.ch

Inkyu Sa
E-mail: inkyu.sa@mavt.ethz.ch

Roland Siegwart
E-mail: rsiegwart@ethz.ch

Juan Nieto
E-mail: nietoj@ethz.ch
Autonomous Systems Lab., ETH Zürich, Zürich, Switzerland

Keywords Informative path planning · Aerial robotics · Environmental monitoring · Remote sensing

1 Introduction

Autonomous mobile robots are increasingly employed to gather valuable scientific data about the Earth. In the past several decades, rapid technological advances have unlocked their potential as a flexible, cost-efficient tool enabling monitoring at unprecedented levels of resolution and autonomy. In many emerging aerial (Ezequiel et al. 2014; Vivaldini et al. 2016; Colomina and Molina 2014) and aquatic (Hitz et al. 2014, 2017; Giridhar and Dudek 2015) applications, these devices are replacing traditional data acquisition campaigns based on static sensors, manual sampling, or conventional manned platforms, which can be unreliable, costly, and even dangerous (Dunbabin and Marques 2012; Manfreda et al. 2018).

The era of robotics-based monitoring has opened many interesting areas of research. A fundamental problem is planning paths to maximize the information gathered about a given environment subject to platform-specific constraints, such as energy, time, or travel distance. This is known as the informative path planning (IPP) problem, which is the subject of much recent work. The main motivation is to trade off map completeness for practical efficiency, as the time for exhaustively monitoring a large area is typically too high to justify a globally optimal solution.

This work focuses on methods for surveying specific terrain characteristics using an aerial robot. A key challenge in this set-up is fusing visual information received from different altitudes into a compact probabilistic map. Using the map, the planning unit must search for

informative trajectories in the large 3-D space above the monitored area, which poses a complex optimization problem. During this procedure, a crucial aspect is trading off between sensor resolution and field of view (FoV), while accounting for limited battery and computational resources. In this paper, we address these issues by presenting a general IPP framework for aerial robots in environmental monitoring applications.

1.1 Contributions

Overall, this article corresponds to a major extension and generalization of the authors' preliminary works (Popović et al. 2017a,b). We present a general approach capable of mapping either discrete or continuous target variables on a terrain using an altitude-dependent sensor. During a mission, the terrain maps built online are used to plan trajectories in continuous 3-D space through a combination of grid search and optimization for maximized information gain. Our method was tested extensively in simulation and validated by mapping a publicly available dataset using an unmanned aerial vehicle (UAV) equipped with an image-based classifier.

The core contributions of this work are:

1. A new framework for mapping and planning informative paths which:
 - is applicable for mapping either discrete or continuous variables on a terrain,
 - generates dynamically feasible trajectories in continuous space,
 - uses a height-dependent noise model to capture sensor uncertainty,
 - can provide any-time solutions, which are useful in real-world adaptive applications.
2. A mapping strategy for IPP which uses Gaussian processes (GPs) as priors for recursively fusing multi-resolution data in constant-time.
3. The extensive evaluation of our framework in simulation and results from a publicly available dataset.

In addition, our implementation is released as an open-source software package¹.

The remainder of this paper is organized as follows. **Section 2** discusses prior studies relevant to our work. We define the IPP problem in **Section 3** and detail our proposed methods for mapping and planning in **Sections 4** and **5**, respectively. Our experimental results are reported in **Section 6**. Finally, in **Section 7**, we conclude with an outlook towards future work.

2 Related work

A large and growing body of literature exists for autonomous information gathering problems. Recently, this field has attracted considerable interest in the context of robotics-based environmental monitoring (Dunbabin and Marques 2012) for a wide variety of applications, including aerial surveillance (Colomina and Molina 2014; Vivaldini et al. 2016), aquatic monitoring (Hitz et al. 2014, 2017), and infrastructure inspection (Ezequiel et al. 2014; Bircher et al. 2016). This section overviews recent work based on two main research streams: (1) methods for environmental modelling; and (2) algorithms for informative planning, or efficient data acquisition.

2.1 Environment mapping

In data gathering scenarios, a model of the environment is fundamental to capture the target variable of interest. Occupancy grids are the most commonly-used representation for spatial sensing with uncorrelated measurements (Elfes 1989). This type of model is suitable for active classification problems with discrete labels, such as occupancy mapping (Charrow et al. 2015) and semantic segmentation (Berrio et al. 2017), and offers relatively high computational efficiency.

However, many natural phenomena exhibit complex interdependencies where the assumption of independent measurements does not hold. A popular Bayesian technique for handling such relationships is using GPs (Rasmussen and Williams 2006). For IPP, they have been applied in various scenarios (Hollinger and Sukhatme 2014; Hitz et al. 2017; Binney and Sukhatme 2012) to collect data accounting for map structure and uncertainty. This framework permits using different kernel functions to express data relations within the environment (Singh et al. 2010) and approximations to scale to large datasets (Rasmussen and Williams 2006). Inspired by Vidal-Calleja et al. (2014), in prior studies, we introduced a GP-based mapping approach for IPP using variable resolution imagery. Our current work extends on these ideas by presenting a general framework that can handle both non-correlated and correlated monitored variables.

2.2 Informative planning

In its most general form, the data gathering task amounts to one of sequential decision-making under uncertainty, which can be expressed as a partially observable Markov decision process (POMDP) (Kaelbling et al. 1998). Unfortunately, despite substantial progress in recent years (Chen

¹ Available at: github.com/ethz-asl/tmplanner.

et al. 2016; Kurniawati et al. 2008), solving large-scale POMDP models remains an open challenge, motivating more efficient solutions.

The NP-hard sensor placement problem (Krause et al. 2008) addresses selecting the most informative measurement sites in a static setting. Discrete planning algorithms, e.g., branch and bound (Binney and Sukhatme 2012), build upon this task by performing combinatorial optimization over a grid. These solvers are typically limited in resolution and scale exponentially with the problem instance. Greedy methods with limited lookahead (Bircher et al. 2016; Chekuri and Pál 2005; Hitz et al. 2014) have been applied to address this issue; however, they tend to converge to locally suboptimal solutions.

Continuous-space planning strategies offer better scalability by leveraging sampling-based methods (Hollinger and Sukhatme 2014) or splines (Vivaldini et al. 2016; Hitz et al. 2017; Charrow et al. 2015; Morere et al. 2017) directly in the robot workspace. As in our prior work (Popović et al. 2017a), we follow the latter approaches in defining smooth polynomial trajectories (Richter et al. 2013) which are optimized globally for an informative objective. Our spline optimization problem set-up most closely resembles the ones studied by Hitz et al. (2017) and Morere et al. (2017); however, our strategy differs in that it uses an informed initialization procedure to obtain faster convergence.

We also distinguish between (i) non-adaptive and (ii) adaptive planning. Non-adaptive approaches, e.g., coverage methods (Galceran and Carreras 2013), explore an environment using a sequence of pre-determined actions. Adaptive approaches (Hitz et al. 2017; Girdhar and Dudek 2015; Lim et al. 2015) allow plans to change as information is collected based on application-specific interests. Sadat et al. (2015) devise an adaptive coverage planner for terrain monitoring applications similar to ours. Their algorithm, however, assumes discrete viewpoints and does not support probabilistic data acquisition. In contrast, our work uses uncertain sensor models for data fusion and performs incremental re-planning in a finite-horizon manner.

3 Problem statement

Our set-up focuses on efficient data-gathering strategies for an aerial robot operating above a terrain. The aim is to maximize the information collected about the environment, while respecting resource constraints, such as energy, time, or distance budgets. Formally, this is known as the IPP problem, which is defined as follows. We seek an optimal trajectory ψ^* in the space of all

continuous trajectories Ψ for maximum gain in some information-theoretic measure:

$$\psi^* = \underset{\psi \in \Psi}{\operatorname{argmax}} \frac{I[\text{MEASURE}(\psi)]}{\text{COST}(\psi)}, \quad (1)$$

s.t. $\text{COST}(\psi) \leq B$.

The function $\text{MEASURE}(\cdot)$ obtains a finite set of measurements along trajectory ψ in the 3-D space above the environment, and $\text{COST}(\cdot)$ provides the corresponding cost, which cannot exceed a predefined budget B . The operator $I[\cdot]$ defines the informative objective quantifying the utility of the acquired measurements.

4 Mapping approach

In this section, we propose a new mapping framework for terrain monitoring applications. The generic structure of our system set-up is depicted in Figure 1. As shown, our framework is capable of mapping either discrete or continuous variables based on measurements extracted from a sensing unit, e.g., a depth or multi-spectral camera. For a particular problem set-up, the map representation can be selected depending on the type of data received. During a mission, the planner uses the terrain maps built online to optimize continuous trajectories for maximum gain in an informative metric reflecting the mission aim. A key aspect of our architecture is its generic formulation, which enables it to adapt to any surface mapping scenario, e.g., elevation (Colomina and Molina 2014), pipe thickness (Vidal-Calleja et al. 2014), gas concentration (Marchant and Ramos 2014), spatial occupancy (O’Callaghan and Ramos 2012), seismic hazards (Gao et al. 2017), post-disaster assessment (Ezequiel et al. 2014), signal strength (Hollinger and Sukhatme 2014), etc.

In Sections 4.1 and 4.2, we present methods of map representation for monitoring discrete and continuous targets, respectively, as the basis of our framework. In Section 5, these concepts are used to formulate the objective function, and we describe our adaptive planning scheme.

4.1 Discrete variable mapping

We study the task of monitoring a discrete variable as an active classification problem. The terrain environment \mathcal{E} is discretized and represented using a 2-D occupancy map \mathcal{X} (Elfes 1989), where each grid cell is associated with an independent Bernoulli random variable indicating the probability of target occupancy (e.g., presence of weed on a farmland). Measurements

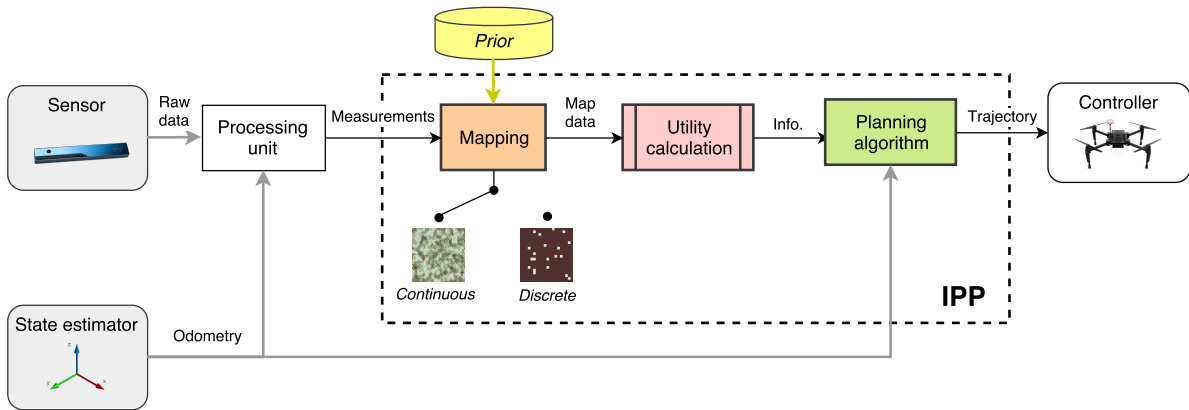


Fig. 1: System diagram showing the key elements of our IPP framework. A map of the target environment is built using measurements extracted from a sensor data stream. At a particular time instant, the map knowledge is used by the planning unit to find the most useful trajectories for data collection, starting at the current pose. These are then executed by the robot, allowing for subsequent map updates in a closed-loop manner.

are taken with a downwards-looking sensor providing inputs to a data processing unit, from which discrete classification labels are obtained. At time t , for each observed cell $\mathbf{x}_i \in \mathcal{X}$ within the FoV from a UAV pose \mathbf{p} above the terrain, a log likelihood update is performed given an observation z :

$$L(\mathbf{x}_i|z_{1:t}, \mathbf{p}_{1:t}) = L(\mathbf{x}_i|z_{1:t-1}, \mathbf{p}_{1:t-1}) + L(\mathbf{x}_i|z_t, \mathbf{p}_t), \quad (2)$$

where $L(\mathbf{x}_i|z_t, \mathbf{p}_t)$ denotes the altitude-dependent inverse sensor model log-likelihood capturing the classification output.

As an example, Figure 2 shows the sensor model for a hypothetical camera-based binary classifier labeling observed cells as “1” (occupied by target) or “0” (target-free). For each class, curves are defined to account for poorer classification with lower-resolution measurements taken at higher altitudes. In practice, these curves can be obtained through a Monte Carlo-type accuracy analysis of raw classifier data by averaging the number of true and false positives (blue and orange curves, respectively) recorded at different altitudes.

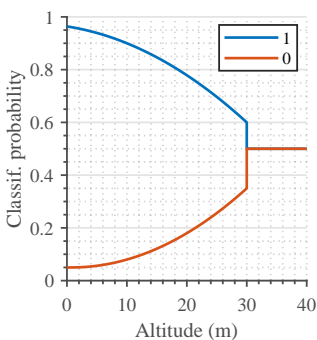


Fig. 2: Sensor model for a typical camera-based binary classifier operating above a terrain. The blue and orange curves depict the probability of observing label “1” or “0”, respectively, i.e., $p(z|\mathbf{x}_i, \mathbf{p})$. As altitude increases, the curves approach unknown classification probability (0.5).

The described approach can be easily extended to mapping multiple class labels by maintaining layers of occupancy maps for each, as demonstrated in Section 6.2.

4.2 Continuous variable mapping

To monitor a continuous variable, our framework leverages a more sophisticated mapping method using GPs to encode spatial correlations common in environmental distributions. We use a GP to initialize a recursive filtering procedure with probabilistic sensors at potentially different resolutions. This approach replaces the computational burden of applying GPs directly with constant processing time in the number of measurements. We describe our method of creating prior maps before detailing the Bayesian data fusion technique.

4.2.1 Gaussian processes

A GP is used to model spatial correlations on the terrain in a probabilistic and non-parametric manner (Rasmussen and Williams 2006). The target variable for mapping is assumed to be a continuous function in 2-D space: $\zeta : \mathcal{E} \rightarrow \mathbb{R}$. Using the GP, a Gaussian correlated prior is placed over the function space, which is fully characterized by the mean $\mu = \mathbb{E}[\zeta]$ and covariance $\mathbf{P} = \mathbb{E}[(\zeta - \mu)(\zeta^\top - \mu^\top)]$ as $\zeta \sim \mathcal{GP}(\mu, \mathbf{P})$, where $\mathbb{E}[\cdot]$ denotes the expectation operator.

Given a pre-trained kernel $K(\mathcal{X}, \mathcal{X})$ for a fixed-size terrain discretized at a certain resolution with a set of n locations $\mathcal{X} \subset \mathcal{E}$, we first specify a finite set of new prediction points $\mathcal{X}^* \subset \mathcal{E}$ at which the prior map is to be inferred. For unknown environments, as in our setup, the values at $\mathbf{x}_i \in \mathcal{X}$ are initialized uniformly with a constant prior mean. For known environments, the GP

can be trained from available data and inferred at the same or different resolutions. The covariance is calculated using the classic GP regression equation (Reece and Roberts 2013):

$$\mathbf{P} = K(\mathcal{X}^*, \mathcal{X}^*) - K(\mathcal{X}^*, \mathcal{X})[K(\mathcal{X}, \mathcal{X}) + \sigma_n^2 I]^{-1} \times K(\mathcal{X}^*, \mathcal{X})^\top, \quad (3)$$

where \mathbf{P} is the posterior covariance, σ_n^2 is a hyperparameter representing signal noise variance, and $K(\mathcal{X}^*, \mathcal{X})$ denotes cross-correlation terms between the predicted and initial locations.

The kernel $K(\cdot)$ determines the generalization properties of the GP model, and is chosen to describe the characteristics of ζ . To describe environmental phenomena, we suggest choosing from among a number of well-known kernel functions common in geostatistical analysis, e.g., the squared exponential or Matérn functions. The free parameters of the kernel function, called hyperparameters, control relations within the GP. These values can be optimized using various methods (Rasmussen and Williams 2006) to match the properties of ζ by training on multiple maps obtained previously at the required resolution.

Once the correlated prior map $p(\zeta|\mathcal{X})$ is determined, independent noisy measurements at variable resolutions are fused as described in the following section.

4.2.2 Sequential data fusion

A key component of our framework is a map update procedure based on recursive filtering. Given a uniform mean and the spatial correlations captured by Equation (3), the map $p(\zeta|\mathcal{X}) \sim \mathcal{GP}(\mu^-, \mathbf{P}^-)$ is used as a prior for fusing new sensor measurements.

Let $\mathbf{z} = [z_1, \dots, z_m]^\top$ denote new m independent measurements received at points $[\mathbf{x}_1, \dots, \mathbf{x}_m]^\top \subset \mathcal{X}$ modelled assuming a Gaussian sensor as $p(z_i|\zeta_i, \mathbf{x}_i) = \mathcal{N}(\mu_{s,i}, \sigma_{s,i})$. To fuse the measurements \mathbf{z} with the prior map $p(\zeta|\mathcal{X})$, we use the maximum *a posteriori* estimator:

$$\operatorname{argmax}_{\zeta} p(\zeta|\mathbf{z}, \mathcal{X}). \quad (4)$$

The Kalman Filter (KF) update equations are applied directly to compute the posterior density $p(\zeta|\mathbf{z}, \mathcal{X}) \propto p(\mathbf{z}|\zeta, \mathcal{X}) \times p(\zeta|\mathcal{X}) \sim \mathcal{GP}(\mu^+, \mathbf{P}^+)$ (Reece and Roberts 2013):

$$\mu^+ = \mu^- + \mathbf{K}\mathbf{v}, \quad (5)$$

$$\mathbf{P}^+ = \mathbf{P}^- - \mathbf{K}\mathbf{H}\mathbf{P}^-, \quad (6)$$

where $\mathbf{K} = \mathbf{P}^- \mathbf{H}^\top \mathbf{S}^{-1}$ is the Kalman gain, and $\mathbf{v} = \mathbf{z} - \mathbf{H}\mu^-$ and $\mathbf{S} = \mathbf{H}\mathbf{P}^- \mathbf{H}^\top + \mathbf{R}$ are the measurement

and covariance innovations. \mathbf{R} is a diagonal $m \times m$ matrix of altitude-dependent variances $\sigma_{s,i}^2$ associated with each measurement z_i , and \mathbf{H} is an $m \times n$ matrix denoting a linear measurement model that intrinsically selects part of the state $\{\zeta_1, \dots, \zeta_m\}$ observed through \mathbf{z} . The information to account for variable-resolution measurements is incorporated according to the measurement model \mathbf{H} in a simple manner as detailed in the following section.

The constant-time updates in Equations (5) and (6) are repeated every time new data is registered. Note that, as all models are linear in this case, the KF update produces the optimal solution. Moreover, this approach is agnostic to the type of sensor used as it permits fusing heterogeneous data into a single grid map.

4.2.3 Altitude-dependent sensor model

As an example, we detail an altitude-dependent sensor model for a downward-facing camera used to take measurements of a terrain, e.g., a farmland or disaster site. In contrast with the pure classification case in Section 4.1, our model needs to express uncertainty with respect to a continuous target distribution. To do this, we consider that the visual data degrades with altitude in two ways: (i) noise and (ii) resolution. The proposed model accounts for these issues in a probabilistic manner as follows.

We assume an altitude-dependent Gaussian sensor noise model. For each observed point $\mathbf{x}_i \in \mathcal{X}$, the camera provides a measurement z_i capturing the target field ζ_i as $\mathcal{N}(\mu_{s,i}, \sigma_{s,i})$, where $\sigma_{s,i}^2$ is the noise variance expressing uncertainty in z_i . To account for lower-quality images taken with larger camera footprints, $\sigma_{s,i}^2$ is modelled as increasing with UAV altitude h using:

$$\sigma_{s,i}^2 = a(1 - e^{-bh}), \quad (7)$$

where a and b are positive constants.

Figure 3 illustrates the sensor noise model used to evaluate our set-up in Section 6 which represents a camera. The measurements z_i denote the levels of the continuous variable being surveyed, e.g., green biomass level or temperature. As for the discrete classifier in Section 4.1, this model can be obtained from the raw analysis of previously acquired datasets at different altitude ranges.

We define altitude envelopes corresponding to different resolution scales with respect to the initial points \mathcal{X} on the map. This is motivated by the fact that the Ground Sample Distance (GSD) ratio (in m/pixel) depends on the altitude of the sensor and its fixed intrinsic resolution. To handle data received from variable altitudes, adjacent \mathbf{x}_i are indexed by a single sensor

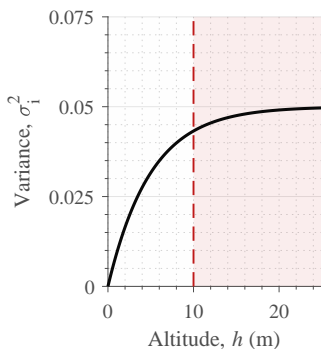


Fig. 3: Inverse sensor noise model for a camera providing measurements as $\mathcal{N}(\mu_{s,i}, \sigma_{s,i})$ with $a = 0.2$, $b = 0.05$ in Equation (7). The uncertainty $\sigma_{s,i}^2$ increases with h to represent degrading image quality. The dotted line at $h = 10$ m indicates the altitude above which image resolution scales down by a factor of 2.

measurement z_i through the measurement model \mathbf{H} . At lower altitudes (higher GSDs, corresponding to the maximum mapping resolution in \mathcal{X}), \mathbf{H} is simply used to select the part of the state observed with a scale of 1. However, at higher altitudes (lower GSDs), the elements of \mathbf{H} used to map multiple ζ_i to a single z_i are scaled by the square inverse of the resolution scaling factor s_f . Note that the fusion procedure described in Section 4.2.2 is always performed at the maximum mapping resolution, so that the proposed model \mathbf{H} considers low-resolution measurements as a scaled average of the high-resolution map.

5 Planning approach

This section details our planning scheme for terrain monitoring. As depicted in Figure 1, we generate fixed-horizon plans to maximize an objective. To do this efficiently, an evolutionary technique is applied to optimize trajectories initialized by a 3-D grid search in the UAV workspace. We first describe our approach to parameterizing trajectories, then detail the algorithm itself.

5.1 Trajectories

A polynomial trajectory ψ is represented by a sequence of N control waypoints to visit $\mathcal{C} = [\mathbf{c}_1, \dots, \mathbf{c}_N]$ connected using $N - 1$ k -order spline segments. Given a reference velocity and acceleration, we optimize the trajectory for smooth minimum-snap dynamics (Richter et al. 2013). The first waypoint \mathbf{c}_1 is clamped as the initial UAV position. As discussed in Section 3, the function MEASURE(\cdot) in Equation (1) is defined by computing the spacing of measurement sites along ψ given a constant sensor frequency and the traveling speed of the UAV along the trajectory.

5.2 Algorithm

A fixed-horizon approach is used to plan adaptively as data are collected. During a mission, we alternate between replanning and execution until the elapsed time t exceeds the budget B . Our replanning approach consists of two stages and is shown in Algorithm 1. First, an initial trajectory, defined by N fixed control points \mathcal{C} , is derived through a coarse grid search (Lines 3-6) in the 3-D workspace. This step proceeds sequentially, selecting points in a greedy manner, so that a rough solution can quickly be obtained. Then, the trajectory is refined to maximize the informative objective. In this step, we employ a generic evolutionary optimization routine (Line 7).

In Algorithm 1, Z symbolizes a general model of the environment \mathcal{E} capturing either a discrete or continuous target variable of interest. The following sections discuss possible objectives for informative planning and outline the key steps of the algorithm.

Algorithm 1 REPLAN_PATH procedure

Input: Current model of the environment Z , number of control waypoints N , lattice points \mathcal{L}
Output: Waypoints defining next polynomial plan \mathcal{C}

- 1: $Z' \leftarrow Z$ // Create a local copy of the map.
- 2: $\mathcal{C} \leftarrow \emptyset$ // Initialize control points.
- 3: **while** $N \geq |\mathcal{C}|$ **do**
- 4: $\mathbf{c}^* \leftarrow$ Select viewpoint in \mathcal{L} using Equation (1)
- 5: $Z' \leftarrow$ PREDICT_MEASUREMENT(Z', \mathbf{c}^*) // From this point.
- 6: $\mathcal{C} \leftarrow \mathcal{C} \cup \mathbf{c}^*$
- 7: $\mathcal{C} \leftarrow$ CMAES(\mathcal{C}, Z) // Optimize polynomial trajectory.

5.3 Utility definition

The utility, or information gain, function I is critical as it encapsulates the specific interests for data-driven planning (Equation (1)). This section discusses possible ways of quantifying the value of new sensor measurements with respect to the proposed map representations.

We examine definitions of I for evaluating the exploratory value of a measurement from a pose \mathbf{p} (Line 4 of Algorithm 1). Note that, above, \mathbf{c} denotes a control waypoint parameterizing a polynomial trajectory, whereas here \mathbf{p} is a specific pose along it from where the measurement was registered. In particular, we consider maximizing the reduction of Shannon's entropy H in the map \mathcal{X} :

$$I[\mathbf{p}] = H(\mathcal{X}^-) - H(\mathcal{X}^+), \quad (8)$$

where the superscripts denote the prior and posterior maps given a measurement taken from \mathbf{p} .

In the discrete variable scenario, the value of H for the occupancy map \mathcal{X} is obtained by simply summing over the entropy values of all cells $\mathbf{x} \in \mathcal{X}$, assuming their independence:

$$H[\mathcal{X}] = - \sum_{\mathbf{x} \in \mathcal{X}} p(\mathbf{x}) \log p(\mathbf{x}) + (1 - p(\mathbf{x})) \log (1 - p(\mathbf{x})), \quad (9)$$

where $p(\mathbf{x})$ indicates the probability of occupancy at \mathbf{x} .

In the continuous variable scenario, however, calculating H involves the determinant of the covariance matrix \mathbf{P} of the GP model (Rasmussen and Williams 2006). We avoid this computationally expensive step by instead minimizing A-optimal information, which only measures the total variance of the map cells (Sim and Roy 2005):

$$I[\mathbf{p}] = \text{Tr}(\mathbf{P}^-) - \text{Tr}(\mathbf{P}^+), \quad (10)$$

where $\text{Tr}(\cdot)$ denotes the trace of a matrix.

We also study an adaptive planning set-up where the objective depends on the values of the measurements taken in addition to their location. This property is very valuable for practical monitoring applications, such as finding function extrema (Marchant and Ramos 2014), classifying level sets (Hitz et al. 2014), or focusing on specific value ranges. To this end, Equation (8) is modified so that the elements mapping to the value of each cell $\mathbf{x}_i \in \mathcal{X}$ are excluded from the objective computation, provided they do not satisfy the requirement which defines interest-based planning.

As an example, in this work, we apply a threshold to an interesting (above) and uninteresting (below) target parameter range. In the discrete case, this simply amounts to computing Equation (8) for the upper set of interesting cells $\mathcal{X}_I = \{\mathbf{x}_i \in \mathcal{X} \mid p_{th} < p(\mathbf{x}_i)\}$, where p_{th} is a threshold on probabilistic occupancy. However, to account for model uncertainty when planning with the GP model (Equation (10)), we adopt the principles of bounded uncertainty-aware classification from (Gotovos et al. 2013; Srinivas et al. 2012). The subset of interesting locations \mathcal{X}_I is defined based on the mean and variance of each cell (μ_i, σ_i) as:

$$\mathcal{X}_I = \{\mathbf{x}_i \mid \mathbf{x}_i \in \mathcal{X} \wedge \mu_i + \beta\sigma_i \geq \mu_{th}\}, \quad (11)$$

where μ_{th} is a threshold on the underlying scalar field and β is a design parameter tuned to scale the confidence interval for classification, i.e., the certainty below μ_{th} a cell must possess before being considered interesting.

Note that Equation (8) defines I for a single measurement site \mathbf{p} . To determine the utility of a complete trajectory ψ , the same principles can be applied by fusing a sequence of measurements and computing the overall information gain.

5.4 3-D grid search

The first step (Lines 3-6 of Algorithm 1) supplies an initial solution for the optimization step in Section 5.5. To achieve this, the planner performs a 3-D grid search based on a coarse multi-resolution lattice \mathcal{L} in the UAV workspace (Figure 4). A low-accuracy solution neglecting sensor dynamics is obtained efficiently by using the points in \mathcal{L} to represent candidate measurement sites and assuming constant velocity travel. Unlike in frontier-based exploration commonly used in cluttered environments (Charrow et al. 2015), selecting goal measurement sites based on map boundaries is not applicable in our set-up. Instead, we conduct a sequential greedy search for N waypoints (Line 3 of Algorithm 1), where the next-best point \mathbf{c}^* (Line 4) is found by evaluating Equation (1) with the chosen utility definition I over \mathcal{L} . For each \mathbf{c}^* , a fused measurement is simulated in \mathcal{X} via Equation (2) or Equation (6) for a discrete or continuous mapping scenario, respectively (Line 5). This point is then added to the initial trajectory solution (Line 6).

As depicted in Figure 4, the length scales of \mathcal{L} can be defined based on the computational resources available and the level of accuracy desired; the denser grid in Figure 4b procures better initial solutions at the expense of longer evaluation times.

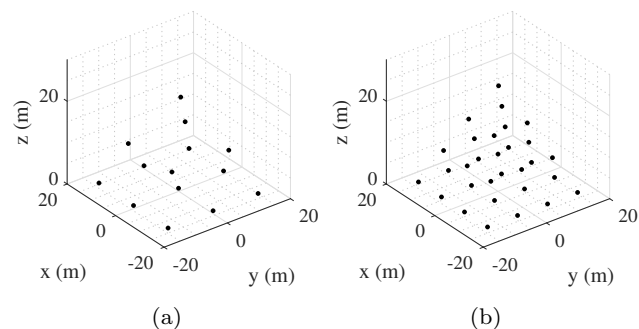


Fig. 4: Visualizations of (a) 14-point and (b) 30-point 3-D lattice grids \mathcal{L} for obtaining an initial trajectory solution in a $40 \times 40 \times 30$ m space. The point density can be chosen to trade-off solution accuracy and computational efficiency in the grid search. Note that the points are sparser at the top due to increasing FoV.

5.5 Optimization

The second step (Line 7 of [Algorithm 1](#)) optimizes the coarse grid search solution for \mathcal{C} by computing \mathbf{I} for a sequence of measurements taken along the trajectory, as defined in [Section 5.3](#). Thereby, the optimizer is initialized with an informed prior to speed up its convergence. Note that this step is agnostic to the optimization method applied; in our specific approach, we apply the Covariance Matrix Adaptation Evolution Strategy (CMA-ES), discussed below. In [Section 6.1.2](#), we evaluate our choice by comparing the use of different routines.

The CMA-ES is a generic global optimization routine based on the concepts of evolutionary algorithms which has been successfully applied to high-dimensional, non-linear, non-convex problems in the continuous domain. As an evolutionary strategy, the CMA-ES operates by iteratively sampling candidate solutions according to a multivariate Gaussian distribution in the search space. Further details, including a convergence analysis, are provided in the in-depth review by [Hansen \(2006\)](#).

Our choice of optimization method is motivated by the non-linearity of the objective space in [Equation \(1\)](#) as well as previous results ([Popović et al. 2017a,b](#); [Hitz et al. 2017](#)). We initialize the mean solution with the grid search result, constraining \mathbf{c}_1 to coincide with the current robot pose, as described above. In addition, a coordinate-wise boundary handling algorithm ([Hansen 2009](#)) is applied to constrain the measurement points to lie within a feasible cubical volume of the workspace above the terrain. For optimization, we use the strategy internal parameters proposed by [Hansen \(2006\)](#), and tune only the population size (number of offspring in the search), co-ordinate wise initial standard deviation (step-size, representing the distribution spread), and maximum number of iterations based on application-specific requirements.

6 Experimental results

This section discusses our experimental findings in both continuous ([Section 6.1](#)) and discrete ([Section 6.2](#)) mapping scenarios. First, in [Section 6.1](#), we evaluate the performance of the proposed approach in simulation and examine the influence of its key parameters. For these experiments, we consider the more complex case of mapping a continuous target variable in a bounded environment using a UAV equipped with an image-based classifier. [Section 6.1.1](#) and [Section 6.1.2](#) compare our approach to state-of-the-art methods and study the effects of using different optimization routines in our al-

gorithm. The adaptive replanning scheme is evaluated in [Section 6.1.3](#). Then, in [Section 6.2](#), we demonstrate the application of our framework on a realistic active classification problem using the RIT-18 dataset ([Kemker et al. 2018](#)).

To begin, [Figure 5](#) presents an illustrative example of the progression of our framework for mapping an *a priori* unknown environment. For adaptive planning, we set a base threshold $\mu_{th} = 40\%$ to focus on the more interesting, higher-valued target parameter range. This value allows us to also include unobserved cells in the objective, which are initialized uniformly with a uninformed mean prior of 50%. The top and bottom rows visualize the planned UAV trajectories and maps, respectively, as images are registered at different times during the mission. [Figure 5-Top-Left](#) depicts the first planned trajectory before (orange) and after (colored gradient) applying the CMA-ES. As shown, the optimization step shifts initial measurement sites (squares) to high altitudes, allowing low-resolution, high-uncertainty data to be quickly collected before the map is refined (second and third columns). A qualitative comparison with ground truth ([Bottom-Right](#)) confirms that our method performs well, producing a fairly complete map in a short time period with most uninteresting regions (hatched areas) identified.

6.1 Simulation results

6.1.1 Comparison against benchmarks

Our framework is evaluated by comparison to benchmarks for continuous variable mapping in a simulated environment. The simulations model a synthetic information gathering problem in a 30×30 m area. The target distributions are generated as 2-D Gaussian random fields with the mapped scalar parameter ranging from 0% to 100% and cluster radii randomly set between 1 m and 3 m. We use a uniform resolution of 0.75 m for both the training X and predictive X^* grids, and perform uninformed initialization with a uniform mean prior of 50%. For the GP, an isotropic Matérn 3/2 kernel is applied. It is defined as ([Rasmussen and Williams 2006](#)):

$$k_{Mat3}(\mathbf{x}, \mathbf{x}^*) = \sigma_f^2 \left(1 + \frac{\sqrt{3}d}{l}\right) \exp\left(-\frac{\sqrt{3}d}{l}\right), \quad (12)$$

where d is the Euclidean distance between inputs \mathbf{x} and \mathbf{x}^* , and l and σ_f^2 are hyperparameters representing the length scale and signal variance, respectively. We train the hyperparameters $\{\sigma_n^2, \sigma_f^2, l\} = \{1.42, 1.82, 3.67\}$ by maximizing the model log marginal likelihood, using

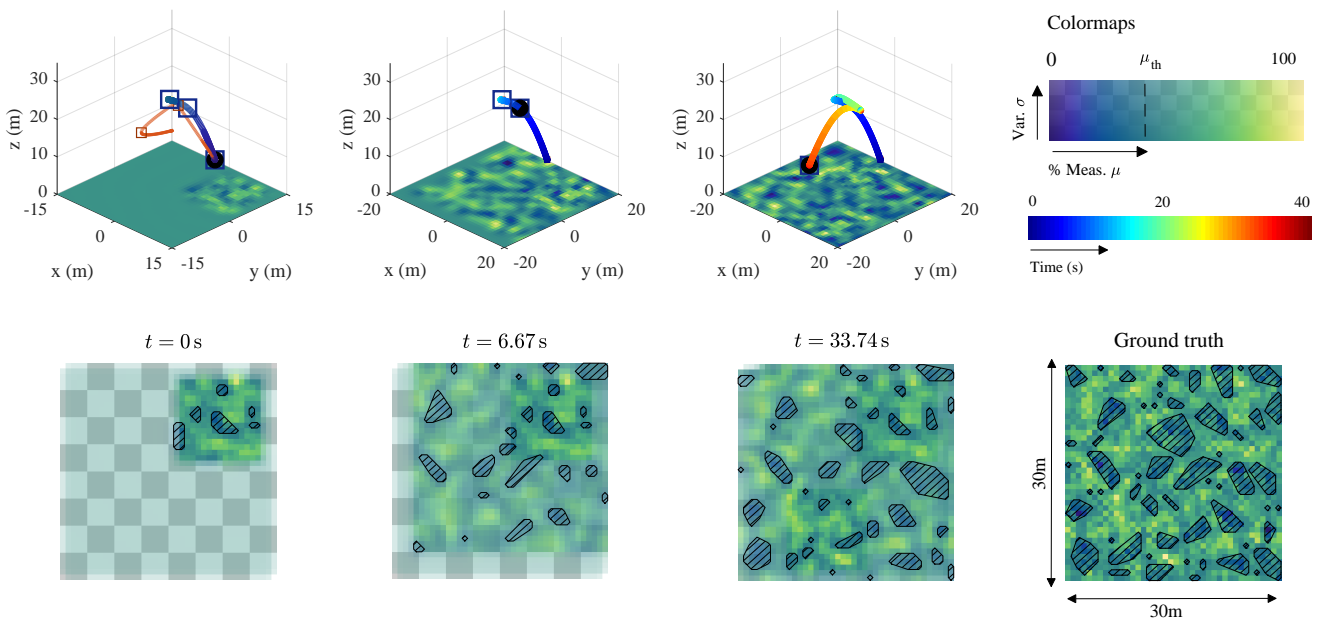


Fig. 5: Example simulation results of our IPP framework. The colormaps are shown on the *Top-Right*. Bluer and yellower shades represent lower and higher values of the target parameter, respectively. In the bottom maps, opacity indicates the model uncertainty (variance, σ_i^2), with the checkerboard added for visual clarity and the hatched sections denoting uninteresting areas with $< \mu_{th} = 40\%$. The ground truth is shown on the *Bottom-Right*. The three columns on the left depict the trajectories (top row) and maps (bottom row) at different snapshots of the mission at times $t = 0$ s, 6.67 s, and 33.74 s. In the top plots, the black dot indicates the current UAV position while the squares show the measurement sites. The *Top-Left* figure illustrates an example trajectory before (orange) and after (colored gradient) optimization using the CMA-ES. Note that the map means are rendered in the top trajectory plots.

4 independent maps with variances modified to cover the entire target parameter range during inference.

For fusing new data, measurement noise is simulated based on the camera model in [Figure 3](#), with a 10 m altitude beyond which images scale by a factor of $s_f = 0.5$. This places a realistic limit on the quality of data that can be obtained from higher altitudes. We consider a square camera footprint with 60° FoV and a 0.15 Hz measurement frequency. For the purposes of these experiments, we assume no actuation or localization noise, and that the on-board camera always faces downwards.

Our approach is compared against three different strategies: (1) traditional “lawnmower” coverage; (2) the sampling-based rapidly exploring information gathering tree (RIG-tree) introduced by [Hollinger and Sukhatme \(2014\)](#), a state-of-the-art IPP method; and (3) naïve random waypoint selection. A 200 s budget B is allocated for all strategies. Considering that, to the best of our knowledge, there is no IPP method that procures optimal results when operating in the continuous trajectory space, we assess performance by comparing different informative metrics during a mission. We quantify uncertainty with the trace of the map covariance matrix $\text{Tr}(P)$ and study the Root Mean Squared Error (RMSE) and Mean Log Loss (MLL) at points in

X with respect to ground truth as accuracy statistics. As described by [Marchant and Ramos \(2014\)](#), the MLL is a probabilistic confidence measure incorporating the variance of the predictive distribution. Intuitively, all metrics are expected to reduce as data are acquired over time, with steeper declines signifying better performance.

We specify the UAV starting position as $(7.5, 7.5)$ m within the field with 8.66 m altitude for all methods to assert the same initial conditions as for the complete coverage pattern. For trajectory optimization, the maximum reference velocity and acceleration are 5 m/s and 2 m/s^2 using polynomials of order $k = 12$, and the number of measurements along a path is limited to 10 for computational feasibility. In our planner, we define polynomials with $N = 5$ waypoints and use the lattice in [Figure 4b](#) for the 3-D grid search. In RIG-tree, we associate control waypoints with vertices, and form polynomials by tracing the parents of leaf vertices to the root. For both planners, we consider the utility I in [Equation \(10\)](#) and set a base threshold of $\mu_{th} = 40\%$ above which map regions are considered interesting.

As outlined in our previous papers ([Popović et al. 2017a,b](#)), we use a finite-horizon version of RIG-tree which alternates between tree construction and plan execution. The branch expansion step-size is set to 10 m

for best performance based on multiple trials. In the coverage planner, height (8.66 m) and velocity (0.78 m/s) are defined for complete coverage given the specified budget and measurement frequency. To design a fair benchmark, we studied possible “lawnmower” patterns with heights determined by the camera FoV. For each pattern, we modified velocity to match the budget, then selected the best-performing one. Finally, in the random planner, we randomly sample a destination in the bounded volume above the terrain and generate a trajectory by connecting it to the current UAV position.

Figure 6 shows how the metrics evolve for each planner during the mission. For our algorithm, we use the CMA-ES optimization method. The coverage curve (green) validates our previous results that uncertainty (left) reduces uniformly and deterministically for a constant altitude and velocity. This motivates IPP approaches, which perform better because they are not limited by a fixed altitude, and can instead compromise between sensor uncertainty and FoV. Both our algorithm (light orange) and RIG-tree (blue) perform better than the random benchmark (dark red), as the latter does not contain an objective function for selecting waypoint destinations.

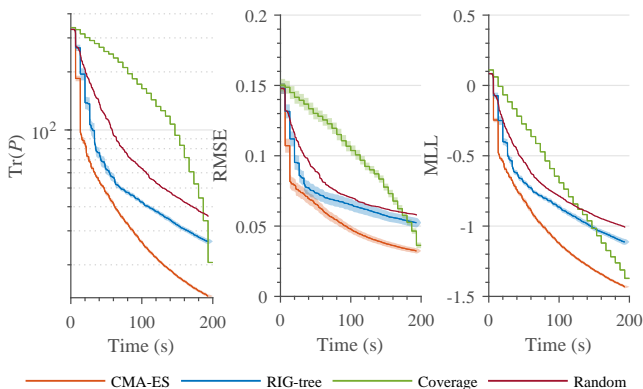


Fig. 6: Comparison of our proposed IPP framework using the CMA-ES against benchmarks for a fixed mission time budget of 200 s. The solid lines represent means over 30 trials. The thin shaded regions depict 95% confidence bounds. Using IPP, map uncertainty (*Left*) and error (*Middle, Right*) reduce quickly as the UAV obtains low-resolution images before descending. Note the logarithmic scale of the $\text{Tr}(P)$ axis.

Our algorithm produces maps with lower uncertainty and error than those of RIG-tree given the same budget. This confirms that our two-stage planner is more effective than sampling-based methods with the proposed mapping strategy. We noted that fixed step-size is a key drawback of RIG-tree, because values allowing initial ascents tend to limit incremental navigation when later refining the map.

Using the same simulation set-up, we also conducted a detailed comparison between our approach and “lawnmower” coverage to examine the benefits of IPP for missions of different durations. First, we considered 6 path budgets B (100, 200, \dots , 600) s, running 10 CMA-ES trials for each. For a given budget, the coverage altitude was chosen for best performance among different complete “lawnmower” patterns, as before. As an example, Figure 7-*Left* depicts the trajectories executed on a 200 s scenario used for the evaluation. The middle graph shows a quantitative analysis of the final achieved map uncertainties ($\text{Tr}(P)$). For comparison, the results of our approach are normalized with the corresponding coverage planner value, so that percentages below 100% (orange line) indicate a better performance of our method. Second, on the right, we compared the mission times required by the two methods to produce maps with the same final uncertainties.

Figure 7 illustrates two key benefits of using our approach: (1) we obtain maps with lower final uncertainty (*Middle*) by not fixing the flight altitude of the UAV; and (2) we attain significant time savings (*Right*) by allowing for the early collection of low-quality data, as evidenced in Figure 6. As a result, with increasing mission time, the marginal discrepancy in the final maps increases. Also, in Figure 7-*Right*, our approach requires substantially less time ($> 50\%$ savings for > 500 s missions) to achieve maps with the same uncertainty. This is because the “zig-zag” pattern for these missions must be set at a lower altitude (6.5 m, compared to 8.66 m for lower budgets) to obtain a reduced sensor noise level, which increases the total distance travelled by the UAV. Interestingly, the coverage path produces a better result only at the end of a 100 s mission; this is because, at this budget, our planner lacks time to descend to refine the map. In future studies, we intend to extend our ideas from previous work (Popović et al. 2017a) and include an awareness of the path budget for planning.

6.1.2 Comparison of optimization methods

Next, we consider the effects of using different optimization routines on the 3-D grid search output in Section 5.5 to evaluate our CMA-ES approach. We use the same simulation set-up as the one described above, i.e., 30 trials for mapping a 30×30 m environment, and study the following methods:

- *Lattice*: 3-D grid search only (i.e., without Line 7 in Algorithm 1),
- *CMA-ES*: global evolutionary optimization routine (Hansen 2006) (described in Section 5.5),

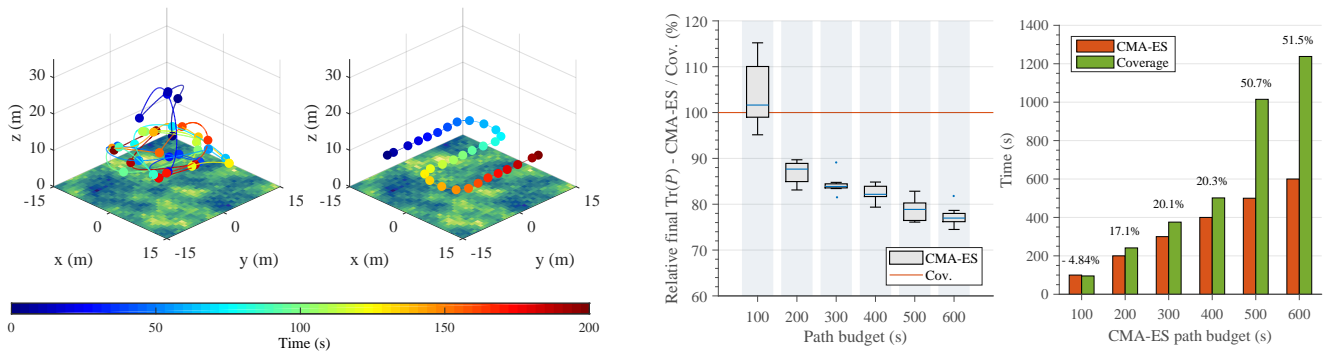


Fig. 7: *Left*: Example of an evaluation scenario comparing our IPP approach with the CMA-ES to “lawnmower” coverage (left and right plots, respectively) for mapping a continuous variable in 200s missions. The colored lines represent the traveled trajectories, the spheres indicate measurement sites, and the ground truth maps are rendered. *Middle*: Comparison of the final map uncertainties ($\text{Tr}(P)$) for various path budgets. Ten CMA-ES trials were run for each budget. *Right*: Comparison of times taken to achieve the same final map uncertainty, given a fixed path budget for the CMA-ES. The orange bars correspond to average values over 10 CMA-ES trials, and relative time savings using our method are shown above the bars in percentages. By allowing for altitude variations, our approach trades off FoV and sensor noise to quickly obtain high-confidence maps with finer end quality in the same time period.

- *Interior Point (IP)*: approximate gradient-based optimization using the interior-point approach (Byrd et al. 2006),
- *Simulated Annealing (SA)*: global optimization based on the physical cooling process in metallurgy (Ingber and Rosen 1992),
- *Bayesian Optimization (BO)*: global optimization using a GP process model (Gelbart et al. 2014).

The aim of these experiments is to examine how the methods compare using standard implementations as baselines. We allocate approximately the same amount of optimization time for each algorithm. For the local IP optimizer, we approximate Hessians by a dense quasi-Newton strategy and apply the step-wise algorithm described by Byrd et al. (2006). For SA, we apply an exponential cooling schedule and an initial temperature of 100. For BO, we use the time-weighted Expected Improvement acquisition function studied by Gelbart et al. (2014) with an exploration ratio of 0.5. Additionally, we examine two variations of the CMA-ES with initial step-sizes of (3, 3, 4) m and (10, 10, 12) m in the (x, y, z) co-ordinates, where the z -axis defines altitude. This allows us to compare different global search behaviors, as the step-size parameter effectively captures how well the problem domain is covered.

Table 1 displays the mean results for each method averaged over the 30 trials, with the benchmarks from Section 6.1.1 included for reference. Suffixes ‘(3, 4)’ and ‘(10, 12)’ denote the smaller and larger step-sizes for the CMA-ES, respectively. Following Marchant and Ramos (2014), we also show weighted statistics to emphasize errors in high-valued regions. As the same objective is used for all methods, consistent trends are observed in both non-weighted and weighted metrics. In Figure 8,

Method	$\text{Tr}(P)$	RMSE	WRMSE	MLL	WMLL
Lattice	56.193	0.0624	0.0622	-0.880	-0.881
CMA-ES (3,4)	46.780	0.0541	0.0536	-0.976	-0.981
CMA-ES (10,12)	50.991	0.0599	0.0596	-0.897	-0.900
IP	51.628	0.0575	0.0574	-0.918	-0.919
SA	55.868	0.0599	0.0595	-0.866	-0.867
BO	62.121	0.0646	0.0642	-0.805	-0.808
RIG-tree	68.581	0.0696	0.0696	-0.755	-0.757
Random	92.681	0.0773	0.0767	-0.668	-0.668
Coverage	165.121	0.0972	0.0972	-0.685	-0.688

Table 1: Mean informative metrics for all optimization methods, averaged over 30 continuous mapping trials. The lowest uncertainties and errors obtained with the CMA-ES justify our proposed global optimization approach.

we show the mean times taken by each method to reduce $\text{Tr}(P)$ to 75% of its initial value to represent the decay speed of the map uncertainty.

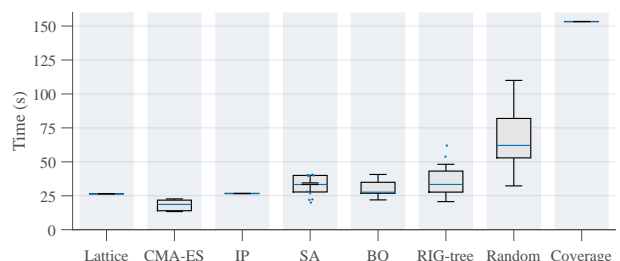


Fig. 8: Mean times required by each optimization method to reduce $\text{Tr}(P)$ (map uncertainty) to 75% of its initial value, averaged over the 30 trials. The CMA-ES result corresponds to a search with smaller step-sizes (‘CMA-ES (3, 4)’). With a mean time of 18.1s, this approach performs best.

Comparing the lattice approach with the CMA-ES and IP methods confirms that optimization reduces both uncertainty and error. With the lowest values, the CMA-ES performs best on all indicators as it searches globally to escape local minima. Using larger step-sizes in ‘CMA-ES (10, 12)’ (> 33% of the workspace extent coordinate-wise) results in worse performance, as these lead to large random fluctuations during the evolutionary search, which slows down convergence. This reflects the importance of selecting suitable step-sizes to cover the application domain, as discussed by Hitz et al. (2017) and Hansen (2006). Surprisingly, applying BO yields mean metrics poorer than those of the lattice. We suspect this to be due to its high exploratory behaviour causing erratic paths similar to those of ‘CMA-ES (10, 12)’. Despite attempting a range of commonly used acquisition functions, we found BO to be the most difficult one to tune for the highly non-linear problem domain.

6.1.3 Adaptive replanning evaluation

Our adaptive replanning scheme is assessed by examining its ability to focus on specific regions of interest in different environments. We consider two continuous mapping scenarios: (1) ‘Split’, handcrafted maps where the interesting area is well-defined; and (2) ‘Gaussian’, the uniformly distributed fields from Section 6.1.1. ‘Split’ maps are partitioned spatially such that half of the cells in \mathcal{X} are classified as interesting based on Equation (11) with a base threshold of $\mu_{th} = 40\%$ and $\beta = 3$. Then we apply these parameters for adaptive replanning in the simulation set-up from Section 6.1.1. The gain of replanning online is evaluated by comparing our approach against itself without an interest-based objective, i.e., treating information acquired from all locations in \mathcal{X} equally. As before, we perform 30 trials in 30×30 m environments.

For a quantitative evaluation, we consider the variations of WRMSE and the uncertainty difference $\Delta\sigma^2$ in the area of interest and the rest of the total area, which is defined by (Hitz et al. 2017) as:

$$\Delta\sigma^2 = \frac{\bar{\sigma}^2(\mathcal{X}_-) - \bar{\sigma}^2(\mathcal{X}_I)}{\bar{\sigma}^2(\mathcal{X}_-)}, \quad (13)$$

where $\bar{\sigma}^2(\cdot)$ evaluates the mean variance and \mathcal{X}_- and \mathcal{X}_I denote the sets of uninteresting and interesting locations, respectively. Note that $\mathcal{X}_- = \mathcal{X} \setminus \mathcal{X}_I$.

Moreover, the rate of uncertainty ($\text{Tr}(P)$) reduction in \mathcal{X}_I evaluates the ability of the planners to focus on interesting regions.

Our results are summarized in Figure 9. As shown qualitatively in Figure 9a, once the uninteresting (bluer)

map side \mathcal{X}_- is classified in a ‘Split’ environment, planning adaptively leads to more measurements on the interesting (yellow) side \mathcal{X}_I , which induces lower final uncertainty in this area, as expected. Figure 9b confirms that, in these scenarios, the relative uncertainty difference $\Delta\sigma^2$ increases more rapidly using adaptivity, while map WRMSE remains low. Note that, early in the mission (< 30 s), both the adaptive and non-adaptive approaches behave similarly to explore the initially unknown map. Finally, Figure 9c shows that the benefit of adaptivity, in terms of reducing uncertainty in areas of interest, is higher in ‘Split’ environments when compared with ‘Gaussian’. Since the region \mathcal{X}_I is clearly distinguished, purely informative measurements can be taken within the camera FoV given the thresholded objective. Planning adaptively, however, yields no disadvantages when the field is uniformly dispersed.

6.2 RIT-18 mapping scenario

We demonstrate our complete framework on a photorealistic scenario in the Gazebo-based RotorS simulation environment (Furrer et al. 2016). In contrast to the preceding section, these experiments show our framework in the discrete mapping domain to reflect the nature of the target dataset. Figure 10 depicts our experimental set-up, which runs on a single desktop with a 2.6 GHz Intel i7 processor and 16 GB of RAM. The planning and mapping algorithms were implemented in MATLAB on Ubuntu Linux and interfaced to the Robot Operating System. For mapping, we use RIT-18 (Kemker et al. 2018), a high-resolution 6-band VNIR dataset for semantic segmentation consisting of coastal imagery along Lake Ontario in Hamlin, NY. In our simulations, the surveyed region is a 200×290 m area featuring the RIT-18 validation fold.

Our UAV model is an AscTec Firefly equipped with a downward-facing camera, which has a 360×480 px image resolution and a $(35.4, 47.2)^\circ$ FoV in the x - and y -directions, respectively. To extract measurements for active classification, we use a modified version of the SegNet convolutional architecture (Badrinarayanan et al. 2017; Sa et al. 2018) accepting multispectral as well as RGB image inputs. The imagery registered from a given UAV pose is passed to the network to produce a dense semantic segmentation output, as exemplified in Figure 11. We simplify the classification problem by only mapping the following 3 classes derived from the RIT-18 labels: (1) ‘Lake’; (2) a combination of ‘Building’, ‘Road Markings’, and ‘Vehicle’ (‘BRV’); and (3) ‘Background’ (‘Bg’), i.e., all others. These particular labels were chosen based on their distributions to obtain

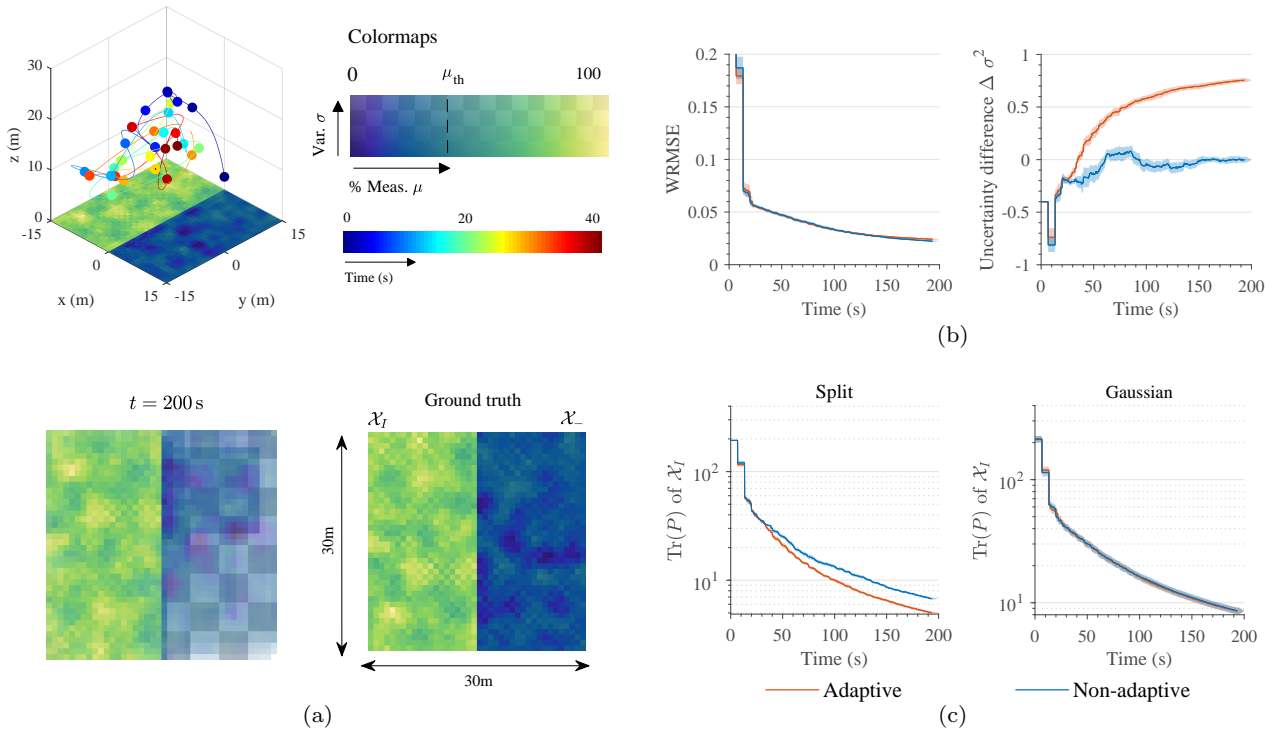


Fig. 9: Evaluation of our adaptive replanning scheme. (a) *Top-Left*: Example ‘Split’ scenario visualizing the trajectory traveled by our planner (colored line) in a 200 s mission. The spheres indicate measurement sites and the ground truth map is rendered. Colormaps are on the *Top-Right*. The dashed line shows the threshold $\mu_{th} = 40\%$ above which map regions are considered interesting (yellow). *Bottom-Left*: Final map output by our planner (left) compared with ground truth (right). The opacity indicates model uncertainty with the checkerboard added for visual clarity. Lower opacity confirms higher certainty in the interesting area \mathcal{X}_I . (b) In ‘Split’ scenarios, adaptivity achieves low error (*Left*) with higher uncertainty differences (*Right*) in interesting areas. (c) In ‘Split’ scenarios (*Left*), adaptivity reduces uncertainty faster in interesting areas, while performing comparably to a standard non-adaptive approach in ‘Gaussian’ scenarios (*Right*). In (b) and (c), the solid lines represent means over 30 trials. The shaded regions depict 95% confidence bounds.

strongly altitude-dependent classification performance, as relevant for the IPP problem set-up.

To model the sensor for predictive planning, we first trained SegNet on all labels using RIT-18 training fold imagery. Our training procedure uses (323, 72, 16) images simulated at 3 different altitudes, (50, 70, 100) m, and is performed on an Nvidia Titan X Pascal GPU module. At 70 m and 100 m, the training images were additionally downsampled to exaggerate the effects of pixel mixing at lower resolutions. Then, classification accuracy was assessed by using validation data to compute confusion matrices at each altitude for the 3 classes of interest (30% train and 70% test split, with a higher proportion of training data at lower altitudes). This enabled us to derive the sensor models in Figure 12, in which we associate intermediate altitudes with the closest performance statistics available. Note that the altitude range considered here is wider compared to the previous sections due to the larger environment size.

We employ a discrete strategy to map the target region, maintaining one independent occupancy grid layer

for each of the 3 classes. Each layer has a uniform resolution of 5 m, and all cells are initialized with an uninformed probability of 0.5. For predictive measurements when planning, we use the sensor models in Figure 12 conditioned on the most probable current map states. For fusing new data, we project the classifier output in Figure 11b on the occupancy grids for each class, performing likelihood updates with the maximum pixel probabilities mapping to each cell. Note that, unlike the pixel-wise classifier output, our mapping strategy does not enforce the probabilities of a cell across the layers to sum to 1, as a cell may contain objects from multiple classes.

The planning goal in this set-up is to efficiently map the ‘BRV’ class, which would be useful, e.g., for identifying man-made features in search and rescue scenarios. Our proposed approach with the CMA-ES is evaluated against the ‘lawnmower’ coverage strategy, considered as the naïve choice of algorithm for such applications. To investigate height-dependent performance, trials are performed with two coverage patterns at fixed altitudes

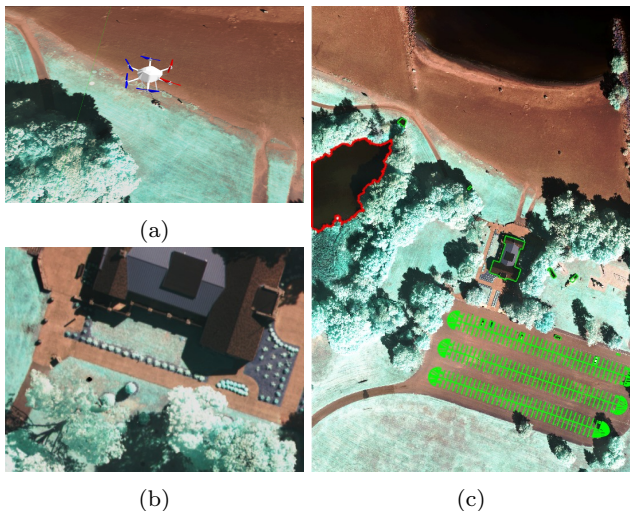


Fig. 10: Our photorealistic simulation set-up in RotorS. (a) and (b) depict the AscTec Firefly UAV and the view from its on-board camera. (c) shows an aerial view of the 200×290 m surveyed area (RIT-18 validation orthomosaic). The red and green lines annotate the two target classes for mapping using our approach: ‘Lake’ and ‘BRV’, respectively.

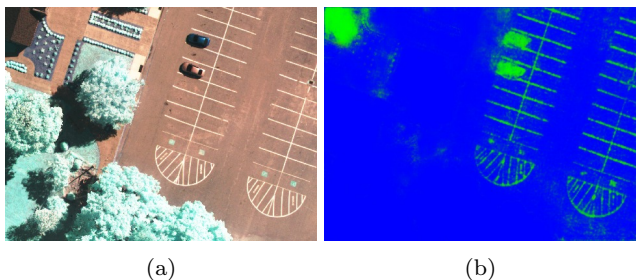


Fig. 11: Example classification result from an altitude of 70 m. (a) shows the RGB image channel input, and (b) visualizes the dense segmentation output. In (b), the probabilistic output for each class [‘Lake’, ‘BRV’, ‘Bg’] is mapped to the corresponding pixel intensity on the [R, G, B] channels.

of 157 m and 104 m, denoted ‘Cvge. 1’ and ‘Cvge. 2’, respectively. In addition, we study both non-adaptive and adaptive versions of our approach, in order to expose the benefits of using adaptive planning to map interesting regions. Our performance metrics are map entropy and RMSE with respect to the RIT-18 ground truth labels.

All methods are given a 400s budget B . To limit computational load on the classifier, we assign a measurement frequency of 0.1 Hz, allowing the UAV to stop while processing images. As before, trajectory optimization is performed on polynomials of order $k = 12$. The UAV starting position in our approach is set as (33, 46) m within the lower-left field corner with 104m altitude to achieve consistency with the lower-altitude coverage pattern. For planning, we use polynomials defined

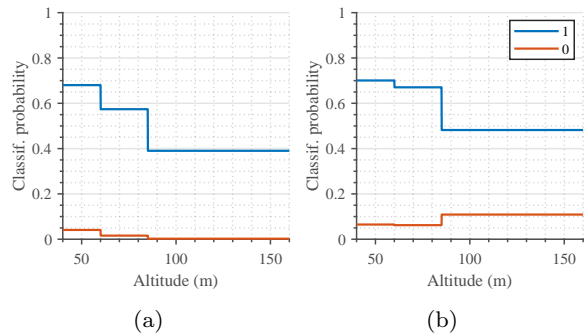


Fig. 12: Sensor models for our trained classifier for the (a) ‘Lake’ and (b) ‘BRV’ classes. The blue and orange curves depict the probability of observing class label “1” or “0”, i.e., true and false positives, respectively. Note that the false positive probability can decrease with altitude as the classifier becomes more conservative with true outputs.

by $N = 5$ waypoints with a reference velocity and acceleration of 15 m/s and 20 m/s². The 3-D grid search is executed on a scaled version of the 30-point lattice in Figure 4b, stretched to cover the rectangular area, and the CMA-ES optimizer runs with initial step sizes of (50, 60, 40) m. To plan adaptively, we apply a low threshold of $p_{th} = 0.4$ in Equation (9) on the occupancy grid layer of the target class. The coverage benchmarks are designed based on the principles discussed in the preceding sections.

Figure 13 compares the performance of each planner in this scenario. As in Section 6.1.1, total map uncertainty reduces uniformly using the coverage patterns, with interesting areas surveyed only towards the end due to the environment layout. In these regions, ‘Cvge. 2’ (dark red) achieves higher-quality mapping than ‘Cvge. 1’ (green) as its lower altitude permits more accurate measurements. This evidences the height-dependent of the classifier, which motivates using IPP to navigate in 3-D space. By planning adaptively using our approach (orange), both uncertainty and error decay most rapidly in the areas of interest, as expected. However, a non-adaptive strategy (blue) performs better in terms of overall map uncertainty, since it is biased towards pure exploration. These results demonstrate how our framework can be tailored to balance exploration (uniform uncertainty reduction) and exploitation (mapping a target class) in a particular scenario.

Figure 14 visualizes the trajectory traveled by our adaptive planner during the mission. As before, the UAV initially (< 100 s) explores unobserved space, before concentrating on high-probability areas for the ‘BRV’ class once they have been discovered (green, or cyan for cells containing both ‘BRV’ and ‘Bg’). It can be seen that the map becomes more complete in these regions

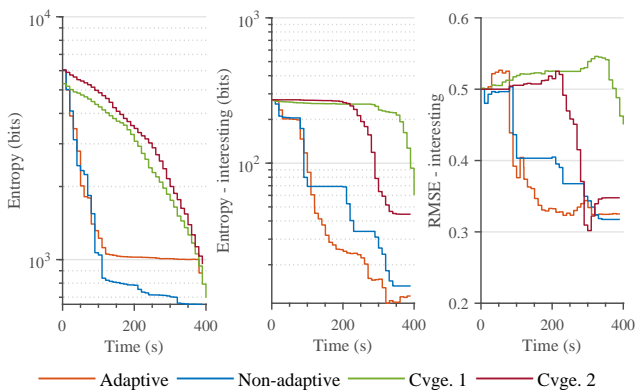


Fig. 13: Comparison of our IPP approach using the CMA-ES against fixed-altitude coverage benchmarks (‘Cvge. 1’ = 157 m, ‘Cvge. 2’ = 104 m) in a 400 s photorealistic mapping scenario. By planning adaptively, map uncertainty (*Middle*) and error (*Right*) in interesting areas (‘BRV’ class) reduce most rapidly, while yielding higher overall map uncertainty (*Left*). Note the logarithmic scale of the Entropy axis.

as low-altitude measurements are accumulated. Note that the two small cars to the right of the building and above the parking lot (visible in Figure 10c) are mapped incorrectly as our SegNet model is limited in segmenting out fine details given the data it was trained on. Considering the richness of the RIT-18 dataset, an interesting direction for future work is to explore different classification methods and target classes within our IPP framework.

7 Conclusion and future work

This paper introduced a general IPP framework for environmental monitoring applications using an aerial robot. The method is capable of mapping either discrete or continuous target variables on a terrain using variable-resolution data received from probabilistic sensors. The resulting maps are employed for IPP by optimizing parameterized continuous-space trajectories initialized by a coarse 3-D search.

Our approach was evaluated extensively in simulations using synthetic and real world data. The results reveal higher efficiency compared to state-of-the-art methods and highlight its ability to efficiently build models with lower uncertainty in value-dependent regions of interest. Furthermore, we validated our framework in an active classification problem using a publicly available dataset. These experiments demonstrated its online application on a photorealistic mapping scenario with a SegNet-based sensor for data acquisition.

The implementation of the proposed planner is released for use and further development by the community along with sample results. Future theoretical work

will investigate scaling the approach to larger environments and extending the mapping model to capture temporal dynamics. This would enable previously acquired data to be used as a prior in persistent monitoring missions. Towards more accurate map building in practice, it would be interesting to also incorporate the robot’s localization uncertainty in the decision-making algorithm.

Acknowledgements We would like to thank Dr. Frank Liebisch for his useful discussions. This project has received funding from the European Unions Horizon 2020 research and innovation programme under grant agreement No 644227 and from the Swiss State Secretariat for Education, Research and Innovation (SERI) under contract number 15.0029.

References

- Badrinarayanan, V., Kendall Alex, and Cipolla, R. (2017). SegNet: A Deep Convolutional Encoder-Decoder Architecture for Image Segmentation. *IEEE Transactions on Pattern Analysis and Machine Intelligence*, 39(12):2481 – 2495.
- Berio, J. S., Ward, J., Worrall, S., Zhou, W., and Nebot, E. (2017). Fusing Lidar and Semantic Image Information in Octree Maps. In *Australasian Conference on Robotics and Automation*, Sydney. ACRA.
- Binney, J. and Sukhatme, G. S. (2012). Branch and bound for informative path planning. In *IEEE International Conference on Robotics and Automation*, pages 2147–2154, Saint Paul. IEEE.
- Bircher, A., Siegwart, R., Kamel, M., Alexis, K., and Oleynikova, H. (2016). Receding horizon path planning for 3D exploration and surface inspection. *Autonomous Robots*.
- Byrd, R. H., Gilbert, J. C., Nocedal, J., Byrd, R. H., Gilbert, J. C., Nocedal, J., Region, A. T., and Based, M. (2006). A Trust Region Method Based on Interior Point Techniques for Nonlinear Programming. *Mathematical Programming*, 89(1):149–185.
- Charrow, B., Liu, S., Kumar, V., and Michael, N. (2015). Information-Theoretic Mapping Using Cauchy-Schwarz Quadratic Mutual Information. In *IEEE International Conference on Robotics and Automation*, pages 4791–4798, Seattle, WA. IEEE.
- Chekuri, C. and Pál, M. (2005). A Recursive Greedy Algorithm for Walks in Directed Graphs. In *IEEE Symposium on Foundations of Computer Science*, pages 245–253. IEEE.
- Chen, M., Frazzoli, E., Hsu, D., and Lee, W. S. (2016). POMDP-lite for Robust Path Planning under Un-

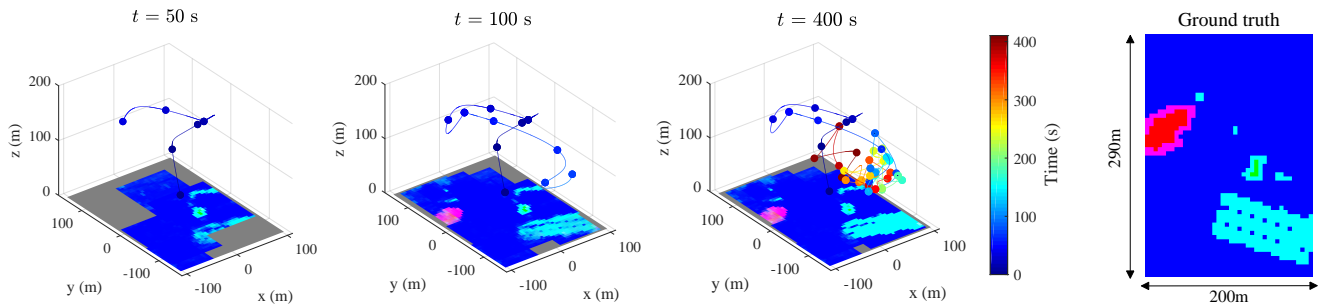


Fig. 14: Visualization of the trajectory traveled by our adaptive planner (colored line) in the 400 s mission. The three plots depict different snapshots of the mission at times $t = 50$ s, 100 s, and 400 s. The RIT-18 ground truth is shown on the right. In the trajectory plots, the spheres indicate measurement sites and the current occupancy map states are rendered. The colors portray composites of the three-layer map representation, with the cell probabilities for each class [‘Lake’, ‘BRV’, ‘Bg’] mapped to the corresponding intensities on the [R, G, B] channels. Gray indicates unobserved space. The sequence shows that our planner quickly explores the area to later focus on more closely mapping interesting regions (‘BRV’ class). Note that the magenta and cyan cells indicate the presence of two classes, [‘Bg’, ‘Lake’] and [‘Bg’, ‘BRV’], respectively.

- certainty. In *IEEE International Conference on Robotics and Automation*, pages 5427–5433.
- Colomina, I. and Molina, P. (2014). Unmanned aerial systems for photogrammetry and remote sensing: A review. *ISPRS Journal of Photogrammetry and Remote Sensing*, 92:79–97.
- Dunbabin, M. and Marques, L. (2012). Robots for environmental monitoring: Significant advancements and applications. *IEEE Robotics and Automation Magazine*, 19(1):24–39.
- Elfes, A. (1989). Using occupancy grids for mobile robot perception and navigation. *Computer*, 22(6):46–57.
- Ezequiel, C. A. F., Cua, M., Libatique, N. C., Tangonan, G. L., Alampay, R., Labuguen, R. T., Favila, C. M., Honrado, J. L. E., Canos, V., Devaney, C., Loreto, A. B., Bacusmo, J., and Palma, B. (2014). UAV Aerial Imaging Applications for Post-Disaster Assessment, Environmental Management and Infrastructure Development. In *International Conference on Unmanned Aircraft Systems*, pages 274–283.
- Furrer, F., Burri, M., Achtelik, M., and Siegwart, R. (2016). RotorS - A Modular Gazebo MAV Simulator Framework. In Koubaa, A., editor, *Robot Operating System (ROS): The Complete Reference (Volume 1)*, pages 595–625. Springer International Publishing, Cham.
- Galceran, E. and Carreras, M. (2013). A survey on coverage path planning for robotics. *Robotics and Autonomous Systems*, 61(12):1258–1276.
- Gao, M., Xu, X., Klinger, Y., Van Der Woerd, J., and Tapponnier, P. (2017). High-resolution mapping based on an Unmanned Aerial Vehicle (UAV) to capture paleoseismic offsets along the Altyn-Tagh fault, China. *Scientific Reports*, 7(1).
- Gelbart, M. A., Snoek, J., and Adams, R. P. (2014). Bayesian Optimization with Unknown Constraints.
- Girdhar, Y. and Dudek, G. (2015). Modeling Curiosity in a Mobile Robot for Long-Term Autonomous Exploration and Monitoring. *Autonomous Robots*, 33(4):645–657.
- Gotovos, A., Casati, N., Hitz, G., and Krause, A. (2013). Active Learning for Level Set Estimation. In *International Joint Conference on Artificial Intelligence*, pages 1344–1350, Beijing. AAAI Press.
- Hansen, N. (2006). The CMA evolution strategy: A comparing review. *Studies in Fuzziness and Soft Computing*, 192(2006):75–102.
- Hansen, N. (2009). A Method for Handling Uncertainty in Evolutionary Optimization With an Application to Feedback Control of Combustion. *IEEE Transactions on Evolutionary Computation*, 13(2):180–197.
- Hitz, G., Galceran, E., Garneau, M.-È., Pomerleau, F., and Siegwart, R. (2017). Adaptive Continuous-Space Informative Path Planning for Online Environmental Monitoring. *Journal of Field Robotics*, 34(8):1427–1449.
- Hitz, G., Gotovos, A., Pomerleau, F., Garneau, M.-È., Pradalier, C., Krause, A., and Siegwart, R. Y. (2014). Fully Autonomous Focused Exploration for Robotic Environmental Monitoring. In *IEEE International Conference on Robotics and Automation*, pages 2658–2664, Hong Kong. IEEE.
- Hollinger, G. A. and Sukhatme, G. S. (2014). Sampling-based robotic information gathering algorithms. *The International Journal of Robotics Research*, 33(9):1271–1287.
- Ingber, L. and Rosen, B. (1992). Genetic Algorithms and Very Fast Simulated Reannealing: A com-

- parison. *Mathematical and Computer Modelling*, 16(11):87–100.
- Kaelbling, L., Littman, M., and Cassandra, A. (1998). Planning and Acting in Partially Observable Stochastic Domains. *Artificial Intelligence*, 101(1-2):99–134.
- Kemker, R., Salvaggio, C., and Kanan, C. (2018). Algorithms for Semantic Segmentation of Multispectral Remote Sensing Imagery using Deep Learning. *ISPRS Journal of Photogrammetry and Remote Sensing*, pages 1–45.
- Krause, A., Singh, A., and Guestrin, C. (2008). Near-Optimal Sensor Placements in Gaussian Processes: Theory, Efficient Algorithms and Empirical Studies. *Journal of Machine Learning Research*, 9:235–284.
- Kurniawati, H., Hsu, D., and Lee, W. S. (2008). SARSOP : Efficient Point-Based POMDP Planning by Approximating Optimally Reachable Belief Spaces. In *Robotics: Science and Systems*, Zürich. MIT Press.
- Lim, Z. W., Hsu, D., and Lee, W. S. (2015). Adaptive informative path planning in metric spaces. *The International Journal of Robotics Research*, pages 1–14.
- Manfreda, S., McCabe, M. F., Miller, P. E., Lucas, R., Madrigal, V. P., Mallinis, G., Dor, E. B., Helman, D., Estes, L., Ciraolo, G., Müllerová, J., Tauro, F., de Lima, M. I., de Lima, J. L., Maltese, A., Frances, F., Caylor, K., Kohv, M., Perks, M., Ruiz-Pérez, G., Su, Z., Vico, G., and Toth, B. (2018). On the Use of Unmanned Aerial Systems for Environmental Monitoring. *Remote Sensing*, 10(4).
- Marchant, R. and Ramos, F. (2014). Bayesian Optimization for Informative Continuous Path Planning. In *IEEE International Conference on Robotics & Automation*, pages 6136–6143, Hong Kong. IEEE.
- Morere, P., Marchant, R., and Ramos, F. (2017). Sequential Bayesian Optimisation as a POMDP for Environment Monitoring with UAVs.
- O’Callaghan, S. T. and Ramos, F. T. (2012). Gaussian process occupancy maps. *The International Journal of Robotics Research*, 31(1):42–62.
- Popović, M., Hitz, G., Nieto, J., Sa, I., Siegwart, R., and Galceran, E. (2017a). Online Informative Path Planning for Active Classification Using UAVs. In *IEEE International Conference on Robotics and Automation*, Singapore. IEEE.
- Popović, M., Vidal-Calleja, T., Hitz, G., Sa, I., Siegwart, R. Y., and Nieto, J. (2017b). Multiresolution Mapping and Informative Path Planning for UAV-based Terrain Monitoring. In *IEEE/RSJ International Conference on Intelligent Robots and Systems*, Vancouver. IEEE.
- Rasmussen, C. E. and Williams, C. K. I. (2006). *Gaussian Processes for Machine Learning*. MIT Press, Cambridge, MA.
- Reece, S. and Roberts, S. (2013). An Introduction to Gaussian Processes for the Kalman Filter Expert. In *FUSION*, pages 1–9.
- Richter, C., Bry, A., and Roy, N. (2013). Polynomial Trajectory Planning for Aggressive Quadrotor Flight in Dense Indoor Environments. In *International Symposium of Robotics Research*, Singapore. Springer.
- Sa, I., Chen, Z., Popović, M., Khanna, R., Liebisch, F., Nieto, J., and Siegwart, R. (2018). weedNet : Dense Semantic Weed Classification Using Multispectral Images and MAV for Smart Farming. In *Robotics and Automation Letters*, Brisbane. IEEE.
- Sadat, S. A., Wawerla, J., and Vaughan, R. (2015). Fractal Trajectories for Online Non-Uniform Aerial Coverage. In *IEEE International Conference on Robotics and Automation*, pages 2971–2976, Seattle, WA. IEEE.
- Sim, R. and Roy, N. (2005). Global A-optimal robot exploration in SLAM. In *IEEE International Conference on Robotics and Automation*, pages 661–666, Barcelona. IEEE.
- Singh, A., Ramos, F., Durrant Whyte, H., and Kaiser, W. J. (2010). Modeling and Decision Making in Spatio-Temporal processes for environmental surveillance. In IEEE, editor, *IEEE International Conference on Robotics and Automation*, pages 5490–5497, Anchorage.
- Srinivas, N., Krause, A., Kakade, S. M., and Seeger, M. W. (2012). Information-Theoretic Regret Bounds for Gaussian Process Optimization in the Bandit Setting. In *IEEE Transactions on Information Theory*, volume 58, pages 3250–3265.
- Vidal-Calleja, T., Su, D., Bruijn, F. D., and Miro, J. V. (2014). Learning Spatial Correlations for Bayesian Fusion in Pipe Thickness Mapping. In *IEEE International Conference on Robotics and Automation*, Hong Kong. IEEE.
- Vivaldini, K. C. T., Guizilini, V., Oliveira, M. D. C., Martinelli, T. H., Wolf, D. F., and Ramos, F. (2016). Route Planning for Active Classification with UAVs. In *IEEE International Conference on Robotics & Automation*.